# Automatic segmentation of right ventricle in cardiac cine MR images using a saliency analysis

Angélica Atehortúa,[1] Maria A. Zuluaga,[2] Juan D. García,[1] and Eduardo Romero[1, a)]
[1)] *Universidad Nacional de Colombia, Bogotá, Colombia*
[2)] *Translational Imaging Group, Centre for Medical Image Computing, University College London, UK*

(Dated: 13 October 2016)

**Purpose:**
Accurate measurement of the right ventricle (RV) volume is important for the assessment of the ventricular function and a biomarker of the progression of any cardiovascular disease. However, the high RV variability makes difficult a proper delineation of the myocardium wall. This paper introduces a new automatic method for segmenting the RV volume from short axis cardiac magnetic resonance images by a salient analysis of temporal and spatial observations.
**Methods:**
The RV volume estimation starts by localizing the heart as the region with the most coherent motion during the cardiac cycle. Afterwards, the ventricular chambers are identified at the basal level using the isodata algorithm, the right ventricle extracted and its centroid computed. A series of radial intensity profiles, traced from this centroid, is used to search a salient intensity pattern that models the inner-outer myocardium boundary. This process is iteratively applied towards the apex, using the segmentation of the previous slice as a regularizer. The consecutive 2D segmentations are added together to obtain the final RV endocardium volume that serves to estimate also the epicardium.
**Results:**
Experiments performed with a public data set, provided by the RV Segmentation Challenge in Cardiac MRI, demonstrated this method is highly competitive with respect to the state of the art, obtaining a Dice score of 0.87, a Hausdorff distance of 7.26 $mm$ while a whole volume was segmented in about 3 $s$.
**Conclusions:**
The proposed method provides an useful delineation of the RV shape using only the spatial and temporal information of the cine MR images. This methodology may be used by the expert to achieve cardiac indicators of the right ventricle function.

Keywords: cardiac cine MR images, heart, profiles, shape and motion analysis

## I. INTRODUCTION

Cardiovascular disease (CD) remains the largest global cause of death, with 17.3 million fatalities per year worldwide[1,2]. This number is expected to rise up to 23.6 million by 2030 due to the influence of factors and habits associated with modern life such as smoking, physical inactivity, obesity, diabetes and stress. The elevated incidence and prevalence of this disease have triggered the alarms of most public health systems which, in consequence, have designed policies oriented to reducing the burden of this disease. Despite these endeavors, many of the CD sufferers will eventually undergo complex treatments aiming to preserve the maximum of cardiac function.

Due to its crucial role in the management of the acute phase of CD, the assessment of the cardiac function dynamics of the left ventricle (LV) has been thoroughly studied[3–5] whereas the role of the right ventricle (RV) has been considered as purely passive. The latter's role has been recently re-evaluated based on evidence that suggests that any LV failure will overload the RV and, therefore, alters its dynamics[6–11]. Nowadays, the RV function constitutes an important biomarker of the progression of any cardiac disease as well as a sensitive prognosis indicator[6].

Since subtle alterations of the right ventricle are practically undetectable in a conventional electrocardiogram, great attention has been paid to different imaging modalities[12–16]. Among these methods, anatomical structures are more clearly visualized with magnetic resonance (MR), during a complete cardiac cycle[7,12,17], i.e., the cardiac chambers and their temporal motion patterns, from which different functional indexes can be computed and integrated to several clinic scenarios. However, quantification of the cardiac cycle requires accurate segmentation of the heart chambers. When performed manually, this process takes around 19 minutes per case[18] and presents high inter-observer variability[19–21].

Semi-automatic and automatic approaches have been developed to obtain accurate and fast RV segmentations[18,22]. Unfortunately, the complex and highly variable anatomical nature of RV make these tasks very difficult. Additionally, the presence of blurry edges

[a)] Electronic mail: edromero@unal.edu.co

may mislead the segmentation algorithm, particularly at the apex level of the ventricle, where the reduced blood flow may result in a non identifiable cavity. In this last case observers are not able to accurately identify nor trace the RV contour. A robust algorithm which is able to overcome these challenges is still not available.

In this paper, a computational framework is proposed to segment the RV volume in short axis (SAX) cine cardiac MRI. The basis of the framework is a simple saliency analysis of the heart which, sequentially and hierarchically, refines the location of the RV. The process can be explained in the following three steps:
First, a **Coarse heart localization**, which locates the region with maximal motion that is known to include all the cardiac structures, reducing the examination area to a region of interest (ROI) that excludes neighboring organs which are not of interest for the present task.
Second, an **Endocardium segmentation**, by far the most complex and error-prone step, is further divided into four sub-tasks:

- Basal ventricle separation, done within the ROI by a simple threshold over the grayscale intensity calculated with the isodata algorithm[23] and *a priori* knowledge about the LV/RV spatial relationship.
- Basal Endocardium delineation, done by searching, along the intensity profiles radiating outwards from the centroid of the RV, for the segments that correspond to the inner-outer myocardium boundary. The selected boundary is the profile segment which best matches a **shape prior**, in this case an upward opening parabola.
- Basal endocardium refinement, by which boundary point outliers are detected and removed and the contour is smoothed.
- Propagation of the basal segmentation towards the apex, computed by repeating the endocardium delineation process in the more apex-wise slices. Previous results, from more basal slices, are used to guide the search.

Third, an **Epicardium estimation**, by dilating the obtained endocardium volume. The method was validated using a cardiac MR data set of 48 subjects provided by the MICCAI 2012 RV Segmentation Challenge in Cardiac MRI (RVSC) [22]. In addition, the proposed strategy was qualitatively assessed on a different database, the Sunnybrook Cardiac Data from a 2009 Left Ventricle Segmentation Challenge.[24].

This paper describes an accurate and fast segmentation of the right ventricle. The method shows high correlations with clinical indexes calculated by manual delineation and demonstrates generalization at obtaining proper segmentations on a second public dataset (LV Segmentation Challenge). Unlike thresholding methods, this approach detects the ventricular wall using exclusively a local intensity model of the ventricles, i.e., instead of taking a global threshold, the algorithm finds out the local patterns that characterize the ventricular wall and sets the particular inner-outer thresholds. An exhaustive radial wise search of this pattern is adapted for each region of the ventricle. As a result, this method does not require a training dataset and is competitive enough in terms of velocity and accuracy. Three main novelties of this method are

1. The exploitation of the temporal information drastically reduces the search of the right ventricular patterns.
2. The RV segmentation is based on a salient model of the ventricular intensity that determines the most probable locations of the inner-outer chamber boundary at a local level
3. the method is also globally regularized by the shape of the ventricle when propagating the first segmented region, the basal slice towards the apex, using always the precedent contour.

The paper is organized as follows: A background of the RV segmentation methods in cardiac MRI is briefly reviewed in Section II. In Section III, the proposed RV volume segmentation approach is described. The experiments and results are provided in Section IV. Finally, discussions and conclusions about the proposed method and associated results are presented in Section V and Section VI respectively.

## II. BACKGROUND

Previous attempts to solve the challenges associated to segmentation of the RV, can be divided into two groups. A first group is the set of methods that need prior information such as multi-atlas based strategies, statistical models and prior propagation. Multi-atlas methods[25–28] register a target case with an atlas database of annotated cardiac images and then somehow fuse annotations of the most similar cases. The registration uses intensity similarity measures and requires to ensure one-to-one correspondences between the target case and the atlas database. These strategies have reported good accuracy results (see Petitjean and Dacher for RV segmentation) as long as the registration ensures a deformation that preserves the topology of the heart structures. As these methods are fully dependent on the variability collected in the database, they may fail when the cardiac structures are very different from the pattern stored in the database. Finally, these methods are computationally very expensive. Statistical models[29,30], similarly to atlas-based approaches, require priors as certain type of pre-defined structures or particular appearances that built up a model to be matched to the target. Statistical models have the advantage of providing a compact representation of the shapes within

a training set. However, as atlas-based methods, they need a large number of samples to capture the RV shape variability. On the other hand, prior propagation methods[31,32] start by a manual segmentation that is propagated to the rest of the cardiac structure. Nevertheless, a proper RV segmentation may be affected by the intrinsic expert variability and the inevitable error propagation.

The second group includes models that need not require prior information. They apply processing techniques directly on the image. Among them, Wang, Peng, and Chen obtained a coarse heart segmentation applying an isodata algorithm after selecting the RV shape as the pixels with more motion, a descriptor that failed when the RV edges were fuzzy. Ringenberg *et al.* combined a window-constrained accumulator threshold method, difference of Gaussians, optimal threshold and morphological operators to segment the RV shape. Mahapatra and Buhmann segmented the RV shape by extracting semantic information using a trained Random Forest classifier. The principal problem with these approaches is that they require a large number of parameters to be tuned and therefore a huge number of cases.

The method herein proposed is part of this second category, i.e., without prior information, furthermore with the advantage of an appropriate estimation of the RV volume with only a few parameters and therefore a low computational cost.

## III. METHOD

The proposed approach segments the RV from SAX images using a cardiac cine MRI and quantifies the RV volume for the whole cycle. The method can be summarized in three steps: (1) A coarse heart localization by determining the region with more motion, reducing the RV search to a smaller region of interest (ROI); (2) segmentation of the right ventricular endocardium borders by performing a 2D hierarchical delineation from basal to apex directions at each time of the cardiac cycle; and (3) estimation of the epicardium contour by dilating the obtained endocardium volume.

All images are pre-processed by remapping intensity values of the slices into the full intensity range $[0, 255]$[36]. These contrast improved images are smoothed with a simple Marr-Hildreth operator[37], i.e., the convolution of the Laplacian of the Gaussian kernel and the original image.

### A. Coarse Heart Localization

The structures surrounding the heart can be excluded from the segmentation process by limiting the ROI to that containing pixels with maximal motion during the whole cycle. This insures an area large enough to contain all the cardiac structures.

The cardiac motion is estimated by computing a saliency map that mimics the center-surround principle[38–41] described for the human visual system, i.e., local features define a level of saliency by their differences with their surroundings. To do so, an estimation of the motion changes per slice $\xi$ is achieved by computing the temporal variations as follows. Given

$$C(\xi) = \{\hat{I}^{\xi}_{t=1}, \hat{I}^{\xi}_{2}, \hat{I}^{\xi}_{3}, .., \hat{I}^{\xi}_{N}\},$$

where $C$ is the temporal sequence of the smoothed images $\hat{I}$ of a slice location $\xi$. The slice $\xi$ at the time $t$ changes with respect to rest of the cycle and $\Delta^{\xi}_{t}$ stores these differences, i.e., this is the set of differences between the image $\hat{I}^{\xi}_{t}$ at the time $t$ and the image $\hat{I}^{\xi}_{k}$ at any other time $k$

$$\Delta^{\xi}_{t} = \left\{\delta^{k}_{t} = |\hat{I}^{\xi}_{t} - \hat{I}^{\xi}_{k}| : \; k = 1, 2, ..., N\right\} \quad \forall\, t = 1, 2, ..., N \tag{1}$$

Once these differences are calculated, a grid of patches (each of $5 \times 5$ pixels ) is superimposed to each $\delta^{k}_{t}$ and the entropy $H$ is calculated for every patch $p$. The local motion estimation is obtained by the sum of local entropies of the same patch along the temporal series of differences $\Delta^{\xi}_{t}$. Higher entropies represent more motion and therefore, higher saliency. The motion saliency map ($MSM$) is defined as

$$MSM(\xi)_{t,p} = \sum_{k=1}^{N} H\left(|\Delta^{\xi}_{t}(\delta_{t,p})|\right) \tag{2}$$

Finally, a binary 2D ROI enclosing the heart for the slice $\xi$ at each phase of the cardiac cycle is obtained after applying a simple Otsu threshold[42] to the $MSM(\xi)_t$ and filling the remaining holes in this binary image, as illustrated in Fig. 1.

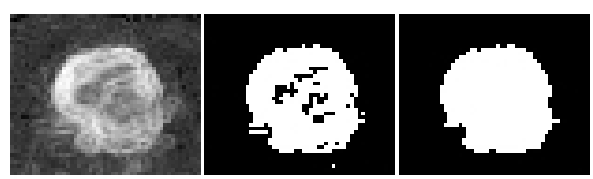

FIG. 1. Coarse heart localization. The left panel displays the obtained motion saliency map (MSM), the center panel shows the binarized MSM, and the right panel shows the final ROI obtained after filling the binary image holes.

### B. Endocardium segmentation

The RV's wall shape depends strongly on the nature of the cardiac pathology and on the patients' characteristics resulting in a high variability in thickness and structure.

Consequently, the delineation of the outermost layer of the RV is usually difficult due to the wall's thickness and the superimposed epicardium fat[43]. Because of this, the proposed algorithm locates the innermost RV layer first and then uses it to guide the segmentation of the RV's outer layer.

The first part of this process consists in delineating the basal slice.

### 1. Basal ventricle separation

Overall, the RV at the basal level is well defined and can be solved as a straightforward segmentation task. At this position, the diastolic and systolic phases represent a large percentage of the whole volume and their segmentation can be used as a starting point for the delineation of the rest of the RV volume, which is independently performed for each phase of the cardiac cycle.

The estimation of the RV boundaries at the basal slice is carried out by a hierarchical approach:

Initially, the ventricular chambers are identified using the isodata algorithm[23] within the ROI (Fig. 2, left panel). The thresholded image suppresses the myocardium and preserves the cardiac cavities. An opening morphological operation reduces the noise of the resultant binary image. The structures of interest, the cardiac chambers, are then selected as the two largest structures that are close the RoI's center of gravity, as illustrated in mid panel of Fig. 2. The obtained coarse ventricular segmentation is displayed in right panel of Fig. 2

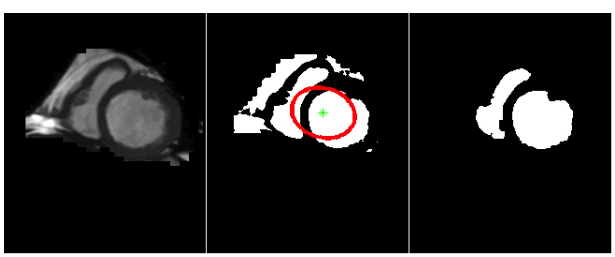

FIG. 2. Localization of the two cardiac chambers, left panel shows the MR image within the ROI. Mid panel illustrates the isodata segmentation and the center of gravity (in green). The two largest structures intersecting an ellipse concentric with the center of gravity are selected. Right panel displays the coarsely segmented ventricles.

### 2. Basal endocardium delineation

Even in the noisier conditions, a trained eye reconstructs a salient version of the myocardium tissue as a thick closed curve. In a polar space $(r, \theta)$, with the curve center as reference, this salience can be inferred if similar intensity radial patterns are observed for neighboring angles. The core of the present work is supported on this observation and after a coarse version of the left and right ventricles is set, the RV boundary is estimated by searching similar patterns in the polar frame defined by the centroid of the initial estimated cardiac chamber.

The myocardium boundary is found out by analyzing the intensity profile along a ray traced from the coarse RV centroid, as illustrated in the top panel of Fig. 3. The lower panel of Fig. 3 shows the intensity profile of such ray. Observe how a first interval of this profile (from 0 to $a$), with little intensity variation, is followed by a second segment (from $a$ to $b$) that resembles an upward opening parabola. This pattern is formed by the intensity drop produced when the ray crosses the inner endocardium and the subsequent rise when the ray reaches the outer epicardium (from $(a, a')$ and $(b, b')$ of the lower panel). These points are easily determined as the major changes of the derivative around the parabola minimum ($(f, f')$). As the range of intensities defined by each of these two ordinates ($a'$ and $b'$) is different, the analysis is performed using the inner parabola branch (from $(a, a')$ to $(f, f')$) since this boundary is always observed. Assuming the wall ventricle intensities are Gaussian distributed and the mean corresponds to the darkest intensity $f'$, it is then reasonable to suppose that the major concentration of dark intensities is within the interval defined by the first standard deviation of the Gaussian, about 68 % of the probability mass. Such value corresponds to the intensities between $f'$ and $m'$, being $m'$ the 32 % of the segment between the minimum $f$ and the branch maximum $a'$, obviously corrected by $f'$. The resultant parabola, shown in blue at the lower panel of Fig. 3, is defined then by three control points ($cp$): the vertex at the minimum intensity value $(f, f')$ and the two branch points defined at $(m, m')$ and $(n, m')$.

There are of course variations from this simple pattern, with the three most common variations illustrated in Fig. 4:

- The simplest pattern is displayed in the top panel of Fig. 4. In this case the three control points are easily determined in the single parabola present. This pattern is characteristic of cardiac images with low noise.

- Center panel in Fig. 4 shows a radial intensity profile with a unique decay (half parabola), usually observed when the epicardium border is blurred or noisy. In this case the criterion is relaxed and only half of the parabola, the one on the endocardium side, is matched with the intensity profile. The epicardium boundary is assumed to be symmetric on the missing (dashed) side.

- Other structures with a similar composition to the myocardium may appear, particularly in pathological conditions. These tissues may appear

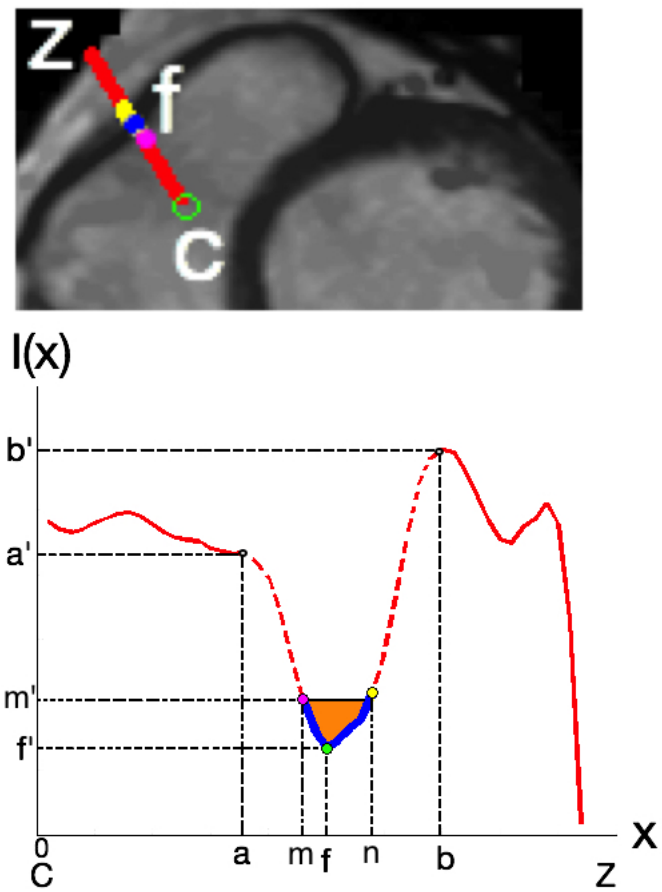


FIG. 3. The top panel illustrates outward radiating segment starting from the centroid $C$ of the RV. The lower panel shows intensity profile values along that ray $CZ$. The parabola pattern in yellow is defined by three control points: The vertex in green, the inner myocardium boundary in magenta and the outer myocardium boundary in blue.

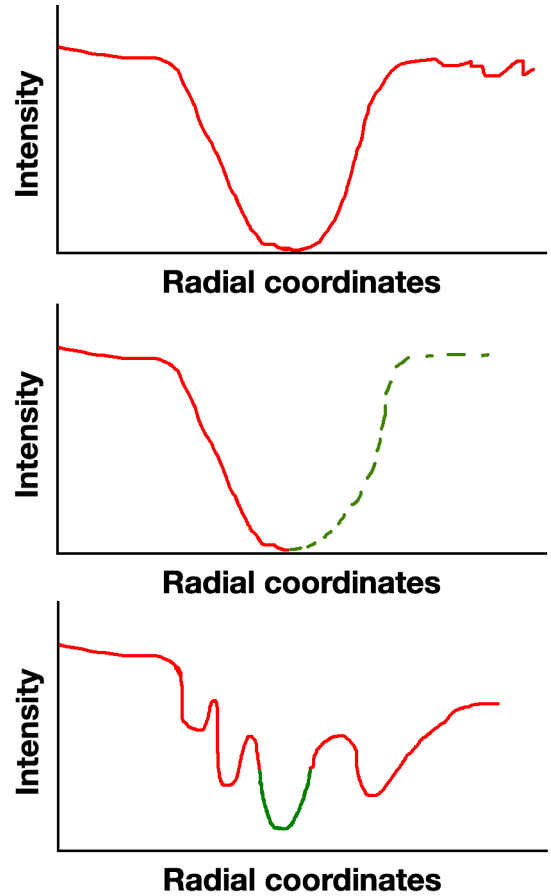


FIG. 4. Different configurations of the radial intensity pattern: A simple profile with a single parabola (top), a fuzzy epicardium border resulting in a half parabola (center) and a profile with multiple possible parabola patterns (bottom).

as multiple parabolas/minimal in the radial profile, as illustrated at the bottom panel of Fig. 4.

Taking these possible configurations into account, the most probable myocardium outline is found as follows.

1. The intensity profile is extracted in all radial directions at $1^o$ steps for every angle $\theta \in [0, 360]$. The method only takes into account those parabolas whose vertex intensity values are below the dynamic range mean. The intensity values of the three control points $I_c(cp_{\theta,k})$ of any found parabola $k$ are systematically stored for every radial profile.

2. If the radial profile matches the trivial cases shown in the top and center panels of Fig. 4, i.e., a unique full or partial parabola, the three control points are easily determined and their intensities stored.

3. When multiple parabola candidates exist, as illustrated in the bottom panel of Fig. 4, the method chooses the one with the best match to the parabolas found in the neighboring radial profiles, minimizing the functional:

$$cp_\beta = \underset{k}{\operatorname{argmin}} \sum_{\theta \in \Theta} \sum_{k \in \Gamma} ||I_c(cp_\theta) - I_c(cp_{\beta,k})||_2 \quad (3)$$

In Equation 3, $cp_\beta$ is the set of searched control points, $\Gamma$ is the number of local minima (parabola candidates) found for the radial profile at a particular angle $\beta$ and $\Theta$ is a neighborhood of the angle $\beta$ composed of the three precedent and posterior profiles. If any of these profiles contains multiple minima, it is removed and replaced with the closest one with a single minimum.

This analysis may miss some segments of the endocardium boundary when rays are parallel to the myocardium wall, as illustrated in the left panel of Fig. 5. Provided that the RV shape is not rounded but rather

an elongated structure attached to the left ventricle, new rays are traced from two reference points $n$ and $m$ that correspond to the centers of two circumferences that best approximate the whole RV coarse shape, as illustrated in the right panel of Fig. 5. A complementary radial analysis consists then in tracing rays from the centers $n$ and $m$, excluding rays that intersected one another within the ROI, as shown in the right panel of the same figure. Observe that no rays are projected neither from $n$ nor $m$ in the arcs delimited by points $r$ and $s$.

The final estimation of the endocardium contour corresponds to the border points found using three different references, $c, n$ and $m$, resulting in a more robust estimation over the boundary. These points, however, may be useful when locating the contour of the next slices in the basal-apex direction.

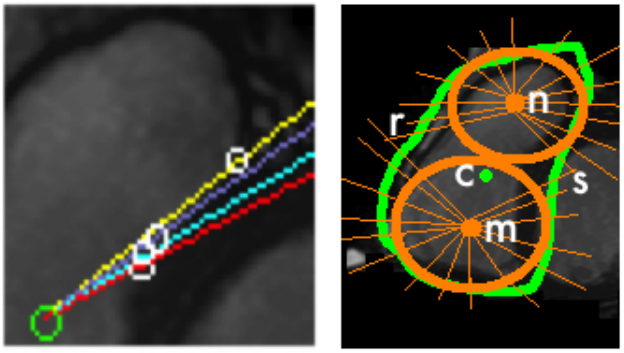


FIG. 5. Left panel zooms out a segment of the RV wall, with the consecutive rays traced from the usual $c$ centroid. Note that a portion of this segment is completely missed by the radial analysis. Right panel shows the rays projected from two points $n$ and $m$, corresponding to the centers of two circumferences that approximate the RV. The whole chamber is covered, but radii from them never intersect one another.

## 3. Basal endocardium refinement

The unidimensional analysis thus far performed can be misled by certain structures like the trabeculae or papillary muscles, resulting in an unsmooth endocardium contour, as illustrated in left panel of Fig. 6. Furthermore, the radial analysis may result in more than one connected segment or in scattered points. These spurious points may be found and removed by mapping the contour to a Normalized Radial Length (NRL) vector $d_\theta$, as described in Tahmasbi, Saki, and Shokouhi[44]. The right panel of Fig. 6 displays the NRL vector of the RV contour at the left panel. Note that the actual contour approximately follows the blue dotted curve, except for some red outliers (right panel of Fig. 6). These red points are removed by applying a local regression to the endocardium NRL contour points. Every point of the endocardium boundary is further adjusted within a small NRL neighborhood. In fact, a second order polynomial regression[45] is applied within an interval iteratively centered at each of the points of the NRL vector $d_\theta$, while varying $\theta$ from $-180°$ to $180°$. The points of the NRL vector minimize the distance to the curve generated by all second order approximations within an interval width that was herein set to a 10 % of the total points. Finally, the NRL vector is mapped back to Cartesian coordinates to obtain the endocardium contour.

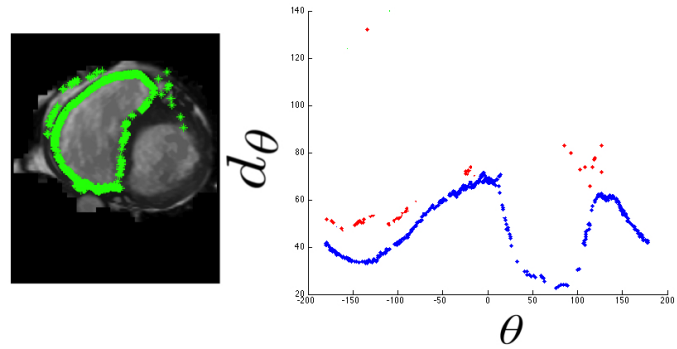


FIG. 6. The points of the endocardium contour are mapped to a Normalized Radial Length (NRL) space $(\theta, d_\theta)$, where inconsistencies are removed. The initial endocardium border points are displayed in the left panel in green and the NRL is shown in the right panel with $d_\theta$ varying from $-180°$ to $180°$.

## 4. Propagation of the basal segmentation towards the apex

The RV volume is the result of the sum of the found areas from each slice multiplied by the inter-slice distance. If one assumes that adjacent slice-to-slice changes are smooth, it is reasonable to expect that a well segmented basal slice should be used by the next slice as a regularizer and that subsequent slices use the precedent one. The overall algorithm is illustrated in Algorithm 1.

**Algorithm 1** Pseudocode for propagation of the basal segmentation towards the apex

**Require:** the endocardium segmentation $\zeta_\xi$ of the basal slice $\xi = 0$
**repeat**
**if** $\zeta_\xi$ centroid $\in$ RoI **then**
$\zeta_{\xi+1} \leftarrow$ by applying the radial analysis of section III B 2 using $\zeta_\xi$ centroid as the reference.
**else**
$\zeta_{\xi+1} \leftarrow$ by applying the radial analysis of section III B 2 using the centroid of the left half of the RoI as the reference.
**end if**
$\zeta_{\xi+1}$ is refined as described in section III B 3
$\zeta_\xi$ is superimposed to the slice $\xi + 1$ and centered around the $\zeta_{\xi+1}$ centroid
$\zeta_{\xi+1} \leftarrow$ is updated by finding the searched pattern which is closer to the $\zeta_\xi$ contour and is defined in section III B 2
$\xi \leftarrow \xi + 1$
**until** $\xi >$ number of slices

### C. Epicardium estimation

Once the whole endocardium volume is estimated, the epicardium is also determined using the endocardium segmentation. To do this, the RV endocardium contour is dilated by a diamond-shaped structuring element of size $\rho$, being $\rho$ the median of the Euclidean distance between the inner and outer myocardium boundary in the third clockwise quadrant, i.e., the free wall of the right ventricle seen from the centroid previously determined. Overall, most dilation operations have been performed using circular structuring elements[34,46,47], while the present investigation used a diamond shaped. This diamond structuring element promoted the propagation of the information exclusively in the normal direction of the ventricular wall.

### D. Data

The performance of the proposed method was tested over a public Cardiac MRI dataset of 48 subjects, supplied by the organizers of the Right Ventricle Segmentation Challenge in MICCAI (RVSC) 2012[22]. The CMR data were acquired from 1.5T short-axis cine CMRI planes, in a plane resolution of 1.3 $mm$, a between-slice distance of 8.4 $mm$, a matrix size of $256 \times 216$ and 20 heart phases for each subject. This data set has been split by the RVSC into three groups: Training, Test 1 and Test 2. Training data consists of a set of 16 cardiac MRI, with equal number of male and female subjects, with an average age of $51 \pm 12$ years. Test 1 dataset was split into 3 women and 13 men cases, with an average age of $48 \pm 18$ years, while test 2 dataset was divided into 5 women and 11 men with an average age of $54 \pm 22$ years. The recorded subjects were diagnosed with several cardiac pathologies namely myocarditis, ischaemic cardiomyopathy, arrhythmogenic right ventricular dysplasia (ARVD), dilated cardiomyopathy, hypertrophic cardiomyopathy, aortic stenosis and cardiac tumour, as well as left ventricular ejection fraction assessment.

For each subject, endocardium and epicardium contours have been delineated by a single observer at the end of the diastole (ED) and the end of the systole (ES).

## IV. RESULTS

### A. Segmentation accuracy

Figure 7 shows the ROI obtained by the motion saliency map on subjects and slices randomly selected from the RVSC dataset.

In spite of the high variability of the test set, as illustrated in Fig. 7, the method successfully encloses the cardiac chamber in these images encompassing heart slices at different levels and times of the cardiac cycle.

A qualitative evaluation of the endocardium segmentation may be observed in Fig. 8. The images present, superimposed, the segmentation and manual delineations for a single subject on different slices and at different moments of the cardiac cycle. Observe how the automatically generated endocardium segmentation is in strong accordance with the manual delineation and follows closely the ventricle boundary. Some parts of the contour at the apex level appear to be slightly displaced (shown in white arrows Fig. 8), particularly at the boundary with the left ventricle. This might be attributed to the high density of the pectinati and papillary muscles next to the left ventricle. A quantitative assessments are the Dice Score[48] (DSC) and the Hausdorff Distance[49] (HD) between the automatic and manual boundaries. The DSC measures the spatial overlap in a range that goes from 0 (no overlap) to 1 (maximum overlap). The HD provides the average distance between the boundaries of the two contours. The Hausdorff measure $\Psi(A, B)$ computes the maximum distance between two sets of points as

$$\Psi(A, B) = \max_{a \in A} \min_{b \in B} ||a - b||_2^2 \tag{4}$$

Table I lists the average and standard deviation of the DSC and HD metrics for the end of diastole (ED) and systole (ES) of the 48 subjects of the RVSC dataset. Although only Test 1 and Test 2 sets are usually used for evaluation, in this work this assessment was extended to the training set (previously described) since the presented method need not require training. Overall, results demonstrate a volume overlap average of about 87 % for the three different experimental groups, with relatively small variances (about 0.1). Overlapping is larger for the diastole, as expected, because of the considerably smaller proportion of papillary muscles and other structures with respect to the perimeter of the chamber wall in this phase of the cycle. That is, the contracted structures form a much more irregular boundary in the systole phase, making this part of the cycle more error-prone. In terms of the HD, which estimates the segmentation compactness or the influence of the local errors, results show a small distance between each point of the automatic contour with respect to the manual delineation, an average of 7.26 $mm$ for a total of 48 cases. Likewise, the epicardium is also segmented and the estimated contours show a slightly better overlapping than the endocardium, probably because the inner structures that contaminate the estimation of the endocardium contour are not longer present. It is important to notice that this estimation allows the ventricular mass to be calculated, a clinical index that most methods never report.

Table II shows a summary of the quantitative reported performance for different methods at the ED and ES,

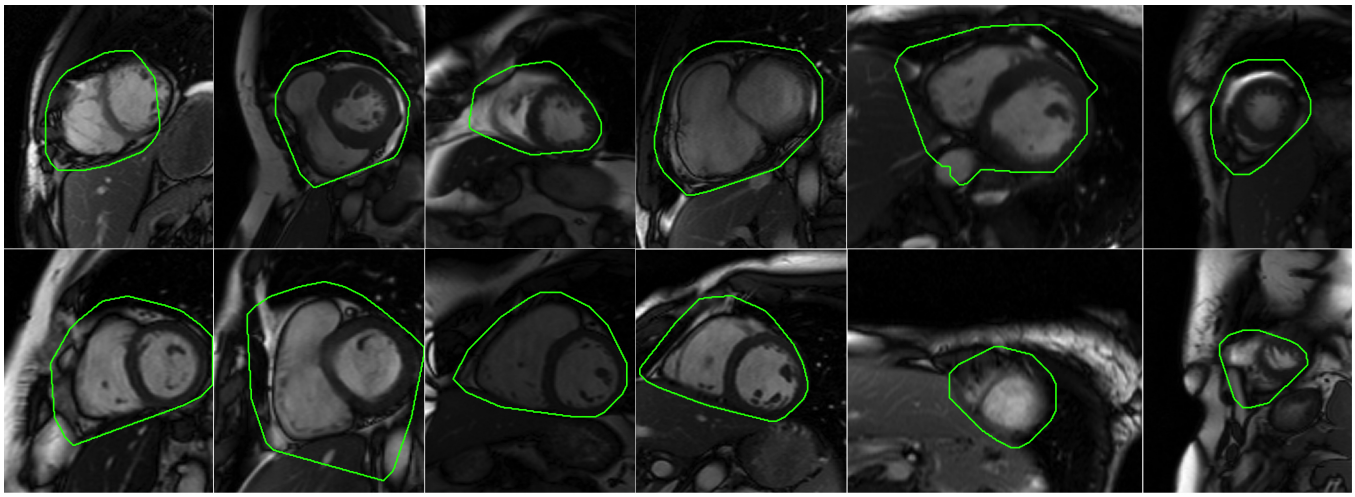

FIG. 7. Each panel corresponds to the coarse heart localization of a random level of the RV volume at a random state of the cardiac cycle of an only subject randomly selected from the RVSC dataset. In all tested images the method consistently locates an ROI containing the whole RV. Although on rare occasions a small portion of the LV is left outside of the ROI, as illustrated in the upper left panel, this does not affect the RV segmentation.

TABLE I. Mean (±standard deviation) of the Dice Score (DSC) and Hausdorff distance (HD, in $mm$) for RV endocardium (Endo) and epicardium (Epi) at the end of the diastole (ED) and end of the systole (ES) using the RVSC dataset.

| | | **Training** | | **Test 1** | | **Test 2** | | **Summary** | |
|---|---|---|---|---|---|---|---|---|---|
| | | **ED** | **ES** | **ED** | **ES** | **ED** | **ES** | **ED** | **ES** |
| Endo | DSC | 0.87 (0.12) | 0.84 (0.12) | 0.87 (0.13) | 0.83 (0.13) | 0.88 (0.13) | 0.84 (0.12) | 0.87 | 0.84 |
| | HD | 6.21 (1.76) | 8.65 (3.40) | 6.30 (1.77) | 8.66 (3.41) | 6.22 (1.72) | 8.59 (3.00) | 6.24 | 8.63 |
| Epi | DSC | 0.89 (0.08) | 0.86 (0.06) | 0.89 (0.09) | 0.87 (0.07) | 0.90 (0.08) | 0.87 (0.06) | 0.89 | 0.87 |
| | HD | 5.59 (1.27) | 8.63 (3.06) | 5.66 (1.29) | 8.64 (3.14) | 5.52 (5.98) | 8.50 (3.32) | 5.59 | 8.59 |

assessed with the same dataset: test 1. One method did not report the epicardium segmentation (N/A). Overall, the presented method outperforms previous works but the results presented by Ringenberg *et al.* at the ED. In this work, Ringenberg *et al.* reported a DSC=0.88 for the endocardium and DSC=0.9 of the epicardium, against a DSC of 0.87 for the endocardium and 0.89 for the epicardium with our method. However, our approach reports a smaller Hausdorff Distance (5.66 against 7.69) and a smaller associated standard deviation. This difference might indicate that the presented method is less prone to be influenced by outliers.

## B. Computation time

The proposed method has been observed to have a very low computational cost, about 3 seconds in average for the whole RV volume segmentation at a particular time $t$, using a Matlab implementation without any optimization. The whole approach was run in a computer with a RAM of 16 $GB$ and a 2.5 $GHz$ intel core i5 processor.

## C. Clinical indexes

To assess the clinical utility of the proposed method, the robustness for computing clinical indexes was calculated. The RV volumes at ED and ES were computed as well as the ejection fraction and the ventricular mass. The RV volumes at the ED (EDV) and the ES (ESV) are obtained using the endocardium slice segmentations, which are then summed and multiplied by the inter-slice gap size. The most important indicator of the RV function, the ejection fraction (EF), is computed as:

$$EF = \frac{EDV - ESV}{EDV} \times 100\% \tag{5}$$

The ventricular mass ($V_M$) is defined as:

$$V_M = density * (EDV_{epi} - EDV_{endo}) \tag{6}$$

being $EDV_{epi}$ and $EDV_{endo}$ the volumes at the ED for epicardium and endocardium tissues, respectively, with a density of 1.05 $g/cm^3$ [52].

Table III shows the correlation coefficients obtained for the linear regressions performed between the automatic

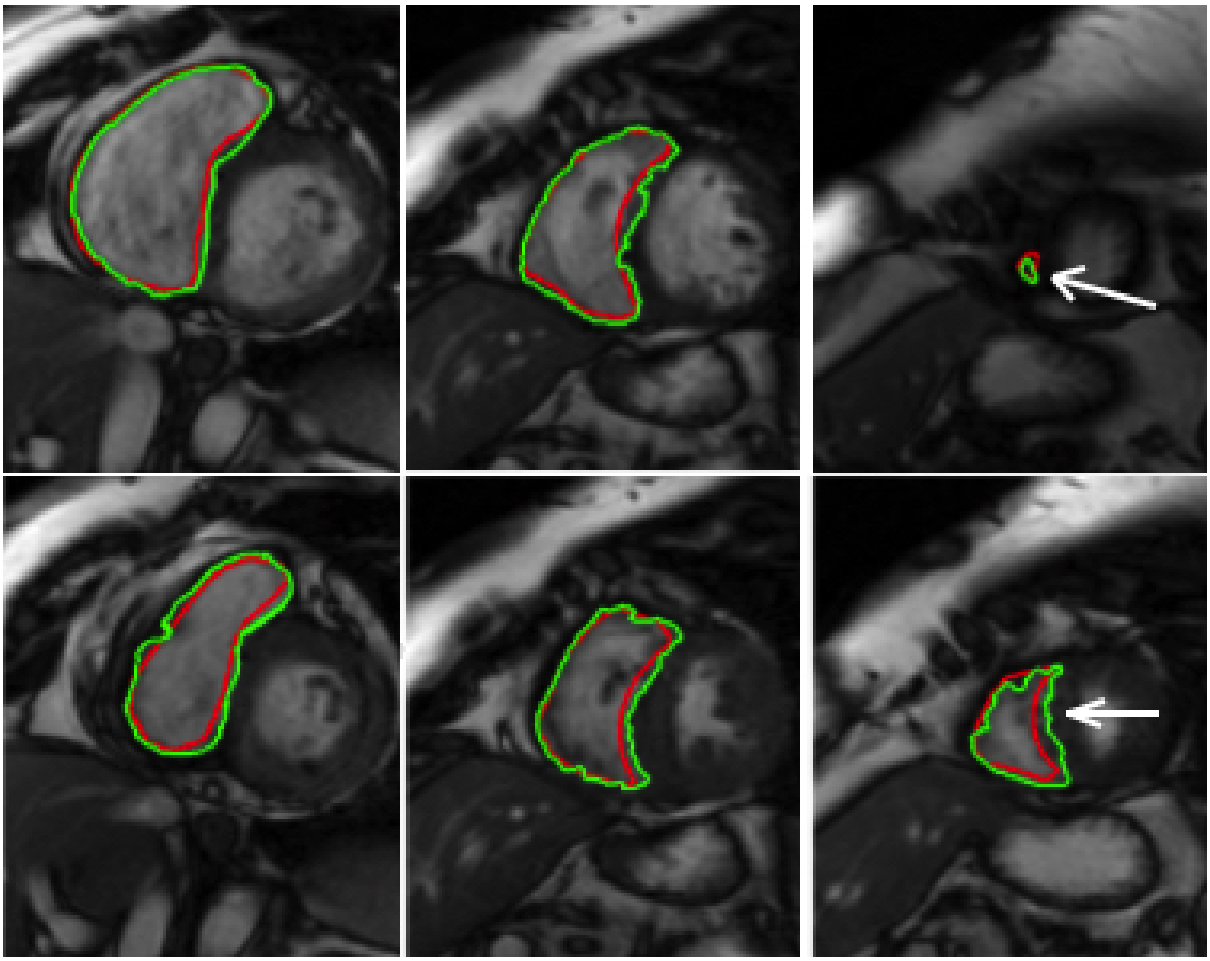

FIG. 8. Figure illustrates the endocardium automatic segmentation (green line) against the manual delineation (red line). Top row shows slices at the end of the diastole while bottom row displays the corresponding slice at the end of the systole. From left to right, panels show the basal, mid and apex levels of the heart segmentation.

TABLE II. Reported mean and standard deviation of several methods (including ours) for the Test 1 set. These results show the Dice Score and Hausdorff metrics (HD in $mm$) for RV endocardium and epicardium at the End of the Diastole (ED) and the End of the Systole (ES)

| **Method** | **End of the Diastole** | | | | **End of the Systole** | | | |
|---|---|---|---|---|---|---|---|---|
| | **Endocardium** | | **Epicardium** | | **Endocardium** | | **Epicardium** | |
| | **DSC** | **HD** | **DSC** | **HD** | **DSC** | **HD** | **DSC** | **HD** |
| | | | | Automatic | | | | |
| **Our method** | 0.87 (0.13) | 5.66 (1.29) | 0.89 (0.09) | 6.30 (1.77) | 0.83 (0.13) | 8.64 (3.14) | 0.87 (0.07) | 8.66 (3.41) |
| Ou et al.[50] | 0.66 (0.24) | 17.66 (8.67) | 0.67 (0.23) | 17.44 (8.51) | 0.53 (0.32) | 20.44 (17.80) | 0.60 (0.30) | 21.91 (18.92) |
| Ringenberg et al.[34] | 0.88 (0.11) | 7.69 (6.03) | 0.90 (0.08) | 8.02 (5.96) | 0.77 (0.18) | 10.71 (7.69) | 0.82 (0.13) | 11.52 (7.70) |
| Wang et al.[33] | 0.63 (0.32) | 22.89 (25.01) | 0.70 (0.34) | 21.45 (25.14) | 0.50 (0.34) | 27.99 (24.97) | 0.55 (0.36) | 27.58 (24.82) |
| Zuluaga et al.[26] | 0.83 (0.17) | 9.77 (7.88) | 0.86 (0.13) | 10.23 (7.22) | 0.72 (0.27) | 11.41 (10.49) | 0.77 (0.23) | 11.81 (9.46) |
| Moolan et al.[51] | 0.86 (0.10) | 8.40 (4.21) | N/A | N/A | 0.75 (0.18) | 10.02 (5.78) | N/A | N/A |
| | | | | Semi-automatic | | | | |
| Bai et al.[47] | 0.86 (0.11) | 7.70 (3.74) | 0.88 (0.08) | 7.93 (3.72) | 0.69 (0.25) | 11.16 (5.53) | 0.77 (0.17) | 11.72 (5.44) |
| Grosgeorge et al.[46] | 0.83 (0.15) | 9.48 (5.41) | 0.86 (0.10) | 9.84 (5.49) | 0.69 (0.23) | 10.56 (5.54) | 0.78 (0.15) | 11.09 (5.34) |
| Punithakumar et al.[31] | N/A | N/A | N/A | N/A | 0.77 (0.16) | 9.64 (4.15) | 0.82 (0.10) | 9.99 (3.85) |

and manual delineations, for each clinical index, namely EDV, ESV, EF and $V_M$ and for the whole RVSC dataset. These coefficients evidence a strong correlation between the automatic and manual contours, with values always larger than a 90%. Table IV illustrates the comparison of these clinical indexes results obtained on the Test1 from

RVSC dataset with other methods of the state of the art.

TABLE III. Clinical indexes results obtained on the RVSC dataset at the ED and the ES frames of the cardiac cycle by computing the correlation coefficient (ideal=1).

| | EDV | ESV | EF | VM |
|---|---|---|---|---|
| Training | 0.98 | 0.98 | 0.95 | 0.93 |
| Test 1 | 0.98 | 0.97 | 0.93 | 0.92 |
| Test 2 | 0.96 | 0.97 | 0.93 | 0.90 |

### D. Application to other datasets

The method was also evaluated with another dataset to illustrate how the proposed strategy is robust to changes of each particular dataset, i.e., it is independent of the capture conditions; an important issue for most models that require a fine tuning phase for each particular acquisition protocol. The data collection provided by the Sunnybrook Health Sciences Center[24], was made publicly available for the Cardiac MR Left Ventricular Segmentation Grand Challenge (MICCAI 2009). From the full set of 45 subjects, 30 were randomly selected for testing, including 24 diagnosed with various cardiac pathologies such as hypertension, cardiac failure or hypertrophic cardiomyopathy. Figure 9 shows the obtained ROIs and endocardium segmentations for different slices, levels and cases. The MSM achieved a correct enclosing the two cardiac chambers for all cases of this dataset. Also observe how, despite the huge shape variability, the strategy locates the right chamber and correctly delineates its boundary. Each image of this figure correspond to a random slice of a random volume of a random subject of this dataset. Observe how the endocardium (green line) contour is properly delineated by our method. Figure 10 illustrates a series 3D surface of the obtained segmentation of the RV endocardial volume during the cardiac cycle of a patient randomly selected.

TABLE IV. Reported clinical indexes results obtained on the Test 1 from RVSC dataset at the ED and the ES frames of the cardiac cycle by computing the correlation coefficient of several methods (including ours).

| METHODS | EDV | ESV | EF | VM |
|---|---|---|---|---|
| Our method | 0.98 | 0.97 | 0.93 | 0.92 |
| Ringengberg et al.[34] | 0.98 | 0.95 | 0.78 | 0.97 |
| Zuluaga et al.[26] | 0.96 | 0.97 | - | - |
| Bai et al.[47] | 0.99 | 0.98 | 0.92 | 0.91 |

## V. DISCUSSION

This paper has introduced a novel and automatic approach to segment the right ventricular chamber in SAX cine MRI. Unlike other RV segmentation methods, this method uses the heart motion to estimate a salient ROI and focuses the exploration on this region. Under a 2D saliency analysis, the endocardium is segmented at every slice at any moment of the cardiac cycle by a local radial search over the intensity profile of a shape prior (parabola) within the salient ROI containing the ventricular structures. The RV basal level is the first slice to be segmented since at this level the right ventricle boundaries tend to be well defined. This first basal segmentation is propagated towards the more noisy slices in the apex direction, using the precedent contour as a reference for the slice segmentation, i.e., the radial search of the prior (parabola) is iteratively performed along the slices and the precedent contour serves as an initial condition of the search. Finally, the epicardium contour is estimated by dilating this endocardium volume.

Results have demonstrated that the present approach is competitive with respect to the techniques of the state of the art. The strategy outperformed the other methods in terms of the HD measure, an estimation of the contour compactness which is very sensitive to local errors. When the DSC measure is used, the proposed method's segmentation accuracy is slightly below ($-0.02$) the results reported by Ringenberg *et al.*. However, in comparison with this approach and other state-of-the-art methods, the present strategy requires no parameter fine tuning, nor previous training or a minimal quantity of data. Other methods demand a strong adjustment of parameters[34,46,51], or are atlas based and, in consequence, computationally expensive and data quantity/quality dependent[26,28,50]. Some authors[31] have used the propagation of a manual segmentation to the rest of the RV, but the dependency on the expert is inevitable and a considerable burden. Other authors[33] have detected the region with maximal motion and selected the RV by a simple threshold. Their reported results, however, are below most state-of-the-art methods. Finally, the computational cost is also a crucial factor of consideration: the present method achieves a complete volume segmentation in approximately $3s$ using non optimal implementation on an ordinary computer.

In the presented method the parameters requiring adjustments were kept to a minimum. The MSM, for instance, uses a classical patch size of $5 \times 5$[53] and consistently detects the cardiac motion in different databases. However, other nearby structures that usually move with the cardiac structures, such as the lung or fragments of the diaphragmatic and pericardium fat , may be incorrectly included in the analysis. As shown in this article, the detection of the two main chambers focuses the analysis and the radial search of the prior, excluding most neighboring tissues.

The interval width for the polynomial regression was also adjusted: The larger the interval width the more points may be removed and the more rigid the obtained curve, whereas the smaller the values the noisier the final curve. A good compromise was found by defining moving intervals and selecting only a ten percent of the contour

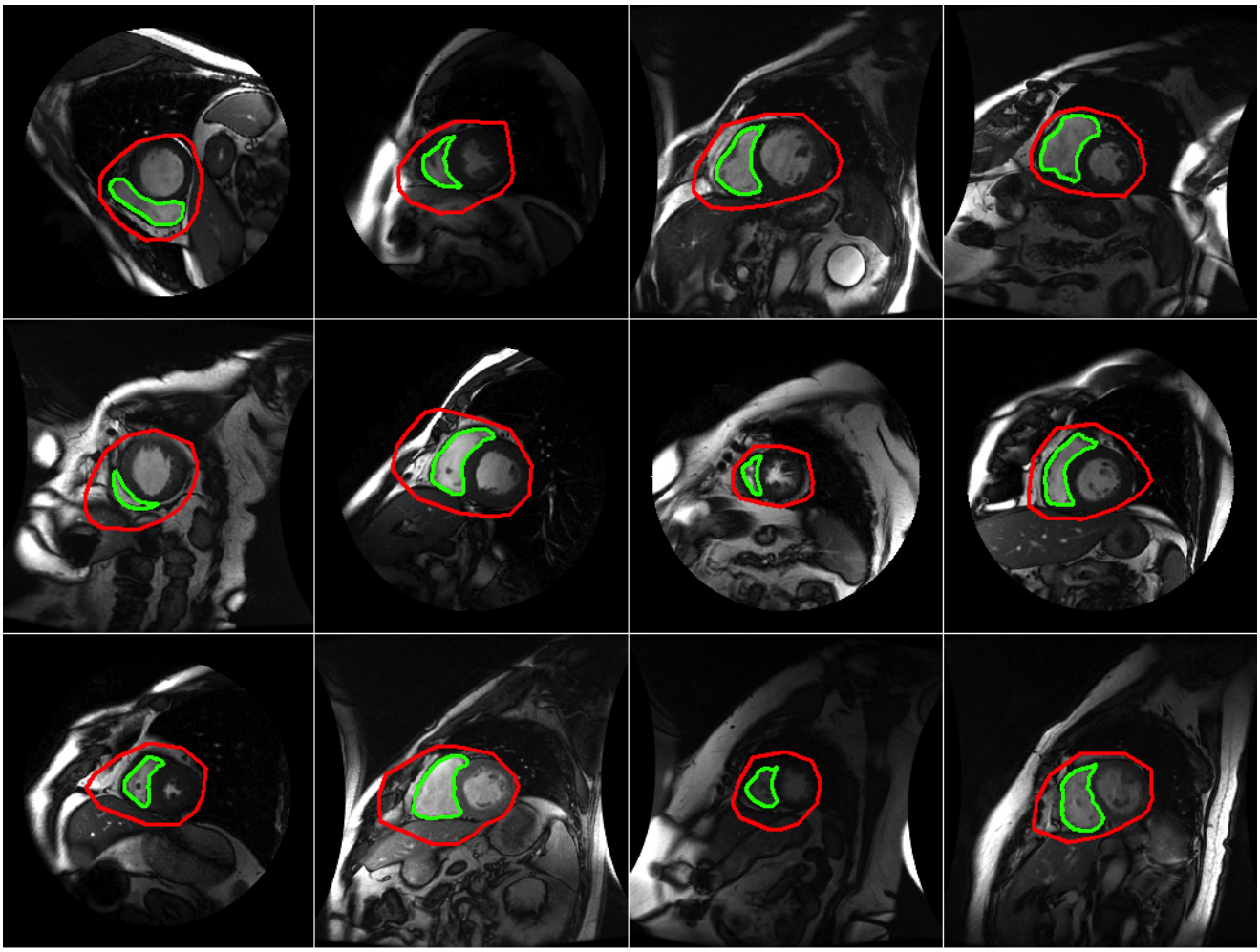

FIG. 9. RV endocardium segmentation for different slices at different phases of the cardiac cycle, where each slice corresponds to a random subject of the Sunnybrook dataset. The endocardium contour is displayed in green line, while the RoI in red line.

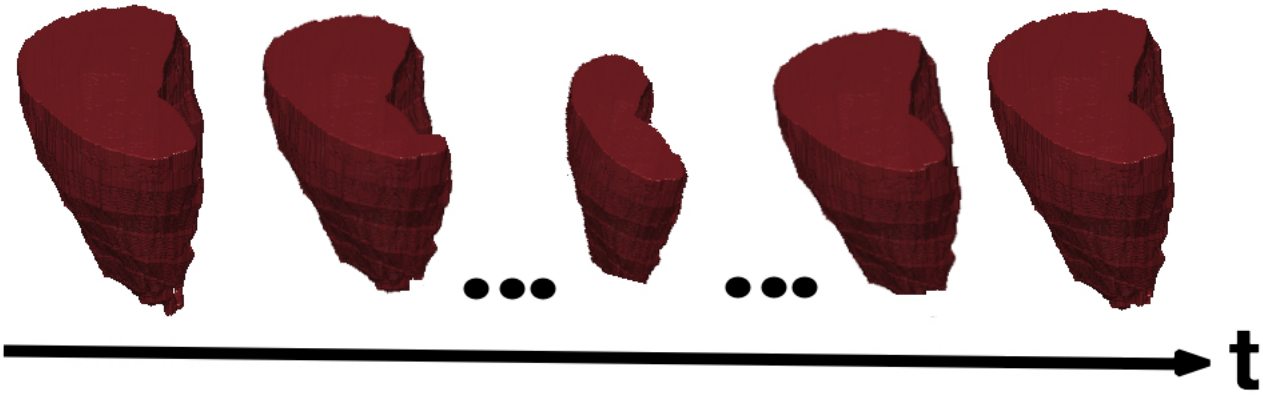


FIG. 10. A series 3D surface data of the obtained segmentation of the RV endocardial volume of a patient during a cardiac cycle.

points at each interval.

Some conditions that may result in a failure of other segmentation approaches are the similarity between the myocardium and its surrounding tissue. This is overcome in the present method by the regularization using the segmentation of the precedent slice. The overlap errors

for the proposed method, calculated using the automatic and the manual delineations, was of about 1.12% for the ED and of 1.5% for the ES.

Wrong estimations of the RV may appear when the wall trabeculation increases. This pattern has been described in pathologies like the right ventricular dilation, RV hypertrophy, idiopathic pulmonary hypertension, Fallot's tetralogy or the cardiac idiopathic dilation, which constitute the group of rare cardiac diseases[6]. These trabeculaes are also salient and might be confused with myocardium. However, these cases could be managed by including a manual correction of the pattern in these very complicated and blurred areas.

The presented method has successfully segmented the RV in SAX views under very different and challenging anatomic and pathological conditions. This approach may be easily extended to segment the left ventricle in CMRI. Future work includes a refinement in the estimation of the myocardium prior by an exhaustive analysis of the myocardium wall in larger populations that include different pathologies.

## VI. CONCLUSIONS

This paper has introduced a novel automatic segmentation strategy to delineate the right ventricle in short axis cine MRI for any phase of the cardiac cycle. The proposed strategy captures most of the cardiac variability without any dependency on the nature of the cardiac pathology. The presented approach achieved an average DSC=0.87 and HD=7.26 $mm$ over 48 real cases, demonstrating that the obtained contours correlate with independent manual delineations. These results suggest this segmentation method may be suitable to support the expert in cine MRI and reduce the inter and intra expert variability.

## ACKNOWLEDGMENTS

This work was supported by Colciencias-Colombia, Grant No. 647 (2015 call for National PhD studies) and a UCL-Santander Research Catalyst Award.

## CONFLICT OF INTEREST DISCLOSURE

The authors have no relevant conflicts of interest to disclose.

[1]World Health Organization, *World health statistics 2010* (World Health Organization, 2010).

[2]D. Mozaffarian, E. J. Benjamin, A. S. Go, D. K. Arnett, M. J. Blaha, M. Cushman, S. de Ferranti, J.-P. Despres, H. J. Fullerton, V. J. Howard, *et al.*, "Heart disease and stroke statistics-2015 update: a report from the american heart association." Circulation **131**, e29 (2015).

[3]R. O. Bonow and J. E. Udelson, "Left ventricular diastolic dysfunction as a cause of congestive heart failure: mechanisms and management," Annals of internal medicine **117**, 502–510 (1992).

[4]K. Swedberg, J. Cleland, H. Dargie, H. Drexler, F. Follath, M. Komajda, L. Tavazzi, O. A. Smiseth, A. Gavazzi, A. Haverich, *et al.*, "Guidelines for the diagnosis and treatment of chronic heart failure: executive summary (update 2005)," European heart journal **26**, 1115–1140 (2005).

[5]M. J. Koren, R. B. Devereux, P. N. Casale, D. D. Savage, and J. H. Laragh, "Relation of left ventricular mass and geometry to morbidity and mortality in uncomplicated essential hypertension," Annals of internal medicine **114**, 345–352 (1991).

[6]N. F. Voelkel, R. A. Quaife, L. A. Leinwand, R. J. Barst, M. D. McGoon, D. R. Meldrum, J. Dupuis, C. S. Long, L. J. Rubin, F. W. Smart, *et al.*, "Right ventricular function and failure report of a national heart, lung, and blood institute working group on cellular and molecular mechanisms of right heart failure," Circulation **114**, 1883–1891 (2006).

[7]F. Haddad, S. A. Hunt, D. N. Rosenthal, and D. J. Murphy, "Right ventricular function in cardiovascular disease, part i anatomy, physiology, aging, and functional assessment of the right ventricle," Circulation **117**, 1436–1448 (2008).

[8]C. R. Greyson, "Evaluation of right ventricular function," Current cardiology reports **13**, 194–202 (2011).

[9]F. Haddad, R. Doyle, D. J. Murphy, and S. A. Hunt, "Right ventricular function in cardiovascular disease, part ii pathophysiology, clinical importance, and management of right ventricular failure," Circulation **117**, 1717–1731 (2008).

[10]J. Kjaergaard, D. Akkan, K. K. Iversen, L. Køber, C. Torp-Pedersen, and C. Hassager, "Right ventricular dysfunction as an independent predictor of short-and long-term mortality in patients with heart failure," European journal of heart failure **9**, 610–616 (2007).

[11]T. G. Di Salvo, M. Mathier, M. J. Semigran, and G. W. Dec, "Preserved right ventricular ejection fraction predicts exercise capacity and survival in advanced heart failure," Journal of the American College of Cardiology **25**, 1143–1153 (1995).

[12]L. Baur, "Magnetic resonance imaging: the preferred imaging method for evaluation of the right ventricle," The international journal of cardiovascular imaging **24**, 699–700 (2008).

[13]S. Kapa, R. Elias, H. J. Connolly, I. S. Syed, and S. J. Asirvatham, "Utility of transthoracic echocardiography to estimate severity of right ventricular dysfunction: an mri comparison study," The international journal of cardiovascular imaging **28**, 251–261 (2012).

[14]R. Krishnamurthy, A. M. Taylor, and C. A. Warnes, "Multimodality imaging guidelines for patients with repaired tetralogy of fallot: a report from the american society of echocardiography," Journal of the American Society of Echocardiography **27**, 111–41 (2014).

[15]M. Francone, "Role of cardiac magnetic resonance in the evaluation of dilated cardiomyopathy: diagnostic contribution and prognostic significance," ISRN radiology **2014** (2014).

[16]M. Pavlicek, A. Wahl, T. Rutz, S. F. de Marchi, R. Hille, K. Wustmann, H. Steck, C. Eigenmann, M. Schwerzmann, and C. Seiler, "Right ventricular systolic function assessment: rank of echocardiographic methods vs. cardiac magnetic resonance imaging," European Heart Journal-Cardiovascular Imaging **12**, 871–880 (2011).

[17]A. M. Crean, N. Maredia, G. Ballard, R. Menezes, G. Wharton, J. Forster, J. P. Greenwood, and J. D. Thomson, "3d echo systematically underestimates right ventricular volumes compared to cardiovascular magnetic resonance in adult congenital heart disease patients with moderate or severe rv dilatation," J Cardiovasc Magn Reson **13**, 78 (2011).

[18]C. Petitjean and J.-N. Dacher, "A review of segmentation methods in short axis cardiac mr images," Medical image analysis **15**, 169–184 (2011).

[19]J. Caudron, J. Fares, P.-H. Vivier, V. Lefebvre, C. Petitjean, and J.-N. Dacher, "Diagnostic accuracy and variability of three semi-quantitative methods for assessing right ventricular systolic function from cardiac mri in patients with acquired heart disease," European radiology **21**, 2111–2120 (2011).

[20]J. Caudron, J. Fares, V. Lefebvre, P.-H. Vivier, C. Petitjean, and J.-N. Dacher, "Cardiac mri assessment of right ventricular function in acquired heart disease: factors of variability," Academic radiology **19**, 991–1002 (2012).

[21]M. G. Danilouchkine, J. J. Westenberg, A. de Roos, J. H. Reiber, and B. P. Lelieveldt, "Operator induced variability in cardiovascular mr: left ventricular measurements and their reproducibility," Journal of Cardiovascular Magnetic Resonance **7**, 447–457 (2005).

[22]C. Petitjean, M. A. Zuluaga, W. Bai, J.-N. Dacher, D. Grosgeorge, J. Caudron, S. Ruan, I. B. Ayed, M. J. Cardoso, H.-C. Chen, *et al.*, "Right ventricle segmentation from cardiac mri: A collation study," Medical image analysis **19**, 187–202 (2015).

[23]T. Ridler and S. Calvard, "Picture thresholding using an iterative selection method," IEEE trans syst Man Cybern **8**, 630–632 (1978).

[24]P. Radau, Y. Lu, K. Connelly, G. Paul, A. Dick, and G. Wright, "Evaluation framework for algorithms segmenting short axis cardiac mri," The MIDAS Journal **49** (2009).

[25]H. A. Kirisli, M. Schaap, S. Klein, S. Papadopoulou, M. Bonardi, C. Chen, A. Weustink, N. Mollet, E. P. A. Vonken, R. van der Geest, T. van Walsum, and W. Niessen, "Evaluation of a multi-atlas based method for segmentation of cardiac CTA data: a large-scale, multicenter, and multivendor study," Medical Physics **37**, 6279–6292 (2010).

[26]M. Zuluaga, M. Cardoso, and S. Ourselin, "Automatic right ventricle segmentation using multi-label fusion in cardiac mri," *Workshop in medical image computing and computer assisted intervention*, (2012).

[27]M. Zuluaga, M. Cardoso, M. Modat, and S. Ourselin, "Multi-atlas propagation whole heart segmentation from mri and cta using a local normalised correlation coefficient criterion," in *Functional Imaging and Modeling of the Heart (FIMH)*, LNCS, Vol. 7945 (2013) pp. 174–181.

[28]W. Bai, W. Shi, D. P. O'Regan, T. Tong, H. Wang, S. Jamil-Copley, N. S. Peters, and D. Rueckert, "A probabilistic patch-based label fusion model for multi-atlas segmentation with registration refinement: application to cardiac mr images," Medical Imaging, IEEE Transactions on **32**, 1302–1315 (2013).

[29]H. Zhang, A. Wahle, R. K. Johnson, T. D. Scholz, and M. Sonka, "4-d cardiac mr image analysis: left and right ventricular morphology and function," Medical Imaging, IEEE Transactions on **29**, 350–364 (2010).

[30]H. El-Rewaidy and A. S. Fahmy, "Segmentation of the right ventricle in mr images using dual active shape model in the bookstein coordinates," in *Biomedical Imaging (ISBI), 2015 IEEE 12th International Symposium on* (IEEE, 2015) pp. 1320–1323.

[31]K. Punithakumar, M. Noga, I. B. Ayed, and P. Boulanger, "Right ventricular segmentation in cardiac mri with moving mesh correspondences," Computerized Medical Imaging and Graphics **43**, 15–25 (2015).

[32]S. Sedai, P. Roy, and R. Garnavi, "Segmentation of right ventricle in cardiac mr images using shape regression," in *Machine Learning in Medical Imaging* (Springer, 2015) pp. 1–8.

[33]C. Wang, C. Peng, and H. Chen, "A simple and fully automatic right ventricle segmentation method for 4-dimensional cardiac mr images," in *Workshop in medical image computing and computer assisted intervention* (2012).

[34]J. Ringenberg, M. Deo, V. Devabhaktuni, O. Berenfeld, P. Boyers, and J. Gold, "Fast, accurate, and fully automatic segmentation of the right ventricle in short-axis cardiac mri," Computerized Medical Imaging and Graphics **38**, 190–201 (2014).

[35]D. Mahapatra and J. M. Buhmann, "Automatic cardiac rv segmentation using semantic information with graph cuts," in *Biomedical Imaging (ISBI), 2013 IEEE 10th International Symposium on* (IEEE, 2013) pp. 1106–1109.

[36]E. F. Arriaga-Garcia, R. E. Sanchez-Yanez, and M. Garcia-Hernandez, "Image enhancement using bi-histogram equalization with adaptive sigmoid functions," in *Electronics, Communications and Computers (CONIELECOMP), 2014 International Conference on* (IEEE, 2014) pp. 28–34.

[37]D. Marr and E. Hildreth, "Theory of edge detection," Proceedings of the Royal Society of London B: Biological Sciences **207**, 187–217 (1980).

[38]L. Itti and C. Koch, "A saliency-based search mechanism for overt and covert shifts of visual attention," Vision research **40**, 1489–1506 (2000).

[39]R. A. Abrams and S. E. Christ, "Motion onset captures attention," Psychological Science **14**, 427–432 (2003).

[40]A. L. Yarbus, *Eye movements during perception of complex objects* (Springer, 1967).

[41]L. Itti, C. Koch, and E. Niebur, "A model of saliency-based visual attention for rapid scene analysis," IEEE Transactions on Pattern Analysis & Machine Intelligence , 1254–1259 (1998).

[42]N. Otsu, "A threshold selection method from gray-level histograms," Automatica **11**, 23–27 (1975).

[43]V. Schejbal, "[epicardial fatty tissue of the right ventricle–morphology, morphometry and functional significance]," Pneumologie (Stuttgart, Germany) **43**, 490–499 (1989).

[44]A. Tahmasbi, F. Saki, and S. B. Shokouhi, "Classification of benign and malignant masses based on zernike moments," Computers in Biology and Medicine **41**, 726–735 (2011).

[45]J. Fox, "Robust regression," An R and S-Plus companion to applied regression (2002).

[46]D. Grosgeorge, C. Petitjean, S. Ruan, J. Caudron, and J.-N. Dacher, "Right ventricle segmentation by graph cut with shape prior," in *3D Cardiovascular Imaging: a MICCAI segementation challenge* (2012) p. xxx.

[47]W. Bai, W. Shi, H. Wang, N. S. Peters, and D. Rueckert, "Multiatlas based segmentation with local label fusion for right ventricle mr images," *Workshop in medical image computing and computer assisted intervention*, **6**, 9 (2012).

[48]L. R. Dice, "Measures of the amount of ecologic association between species," Ecology **26**, 297–302 (1945).

[49]D. P. Huttenlocher, G. A. Klanderman, and W. J. Rucklidge, "Comparing images using the hausdorff distance," Pattern Analysis and Machine Intelligence, IEEE Transactions on **15**, 850–863 (1993).

[50]Y. Ou, J. Doshi, G. Erus, and C. Davatzikos, "Multi-atlas segmentation of the cardiac mr right ventricle," Proceedings of 3D Cardiovascular Imaging: A MICCAI Segmentation Challenge. Nice, France (2012).

[51]O. Moolan-Feroze, M. Mirmehdi, M. Hamilton, and C. Bucciarelli-Ducci, "Segmentation of the right ventricle using diffusion maps and markov random fields," in *Medical Image Computing and Computer-Assisted Intervention–MICCAI 2014* (Springer, 2014) pp. 682–689.

[52]F. Grothues, G. C. Smith, J. C. Moon, N. G. Bellenger, P. Collins, H. U. Klein, and D. J. Pennell, "Comparison of interstudy reproducibility of cardiovascular magnetic resonance with two-dimensional echocardiography in normal subjects and in patients with heart failure or left ventricular hypertrophy," The American journal of cardiology **90**, 29–34 (2002).

[53]P. Coupé, J. V. Manjón, V. Fonov, J. Pruessner, M. Robles, and D. L. Collins, "Patch-based segmentation using expert priors: Application to hippocampus and ventricle segmentation," NeuroImage **54**, 940–954 (2011).